Supplementary Information (SI) for ChemComm.

Melt quenched synthesis of a manganese ZIF glass

Luis León-Alcaide,[a] Alberto Fernández-Alarcón,[a] Joaquín Calbo,[a] David A. Keen,[b] and Guillermo Mínguez Espallargas[a]*

[a] Instituto de Ciencia Molecular (ICMol), Universidad de Valencia, c/ Catedrático José Beltrán, 2, 46980, Paterna, Spain

[b] ISIS Facility, Rutherford Appleton Laboratory, Harwell Campus, Didcot, Oxfordshire OX11 0QX, United Kingdom

Supporting Information

Contents

S1. Methods

All reagents were commercially available and used without further purification.

Synthesis of MUV-44(mog): Bis(tetramethylcyclopentadienyl)manganese (II) (44.6 mg, 0.15 mmol) and imidazole (20.4 mg, 0.3 mmol) were combined in a vacuum-sealed 4 mm diameter layering tube. The mixture was heated to 150 °C for four days, yielding white crystals suitable for single-crystal X-ray diffraction. Unreacted starting materials were removed by acetonitrile extraction, leaving pure **MUV-44(mog)** as white crystals, confirmed by powder X-ray diffraction. The entire procedure is carried out inside a glove box to prevent oxidation.

Synthesis of MUV-44(dia-c): Approximately 15 mg of **MUV-44(mog)** was subjected to a thermal process: a 15-minute hold at 40 °C, heating to 300 °C with a 10-minute isotherm, and then cooling to 25 °C. The heating and cooling rates were maintained at 10 °C min^{-1}.

Synthesis of MUV-44(zni): Approximately 15 mg of **MUV-44(mog)** was subjected to a thermal process: a 15-minute hold at 40 °C, heating to 400 °C with a 10-minute isotherm, and then cooling to 25 °C. The heating and cooling rates were maintained at 10 °C min^{-1}.

Synthesis of a_g-MUV-44: Approximately 15 mg of **MUV-44(mog)** underwent a thermal treatment following this profile: initial hold at 40 °C for 15 minutes, followed by heating to 475 °C with a 10-minutes isotherm, and then cooling down to 25 °C. Both heating and cooling rates were maintained at 10 °C min^{-1}.

Single-Crystal X-ray Diffraction: A single crystal of **MUV-44(mog)** was mounted on a glass fiber using a viscous hydrocarbon oil. The crystal was then transferred directly into a cold nitrogen stream for data collection. X-ray diffraction data were collected at 120 K on a DW rotating anode synergy R diffractometer using Cu-K_α radiation (λ = 1.54184 Å). Data processing was performed using the CrysAlisPro suite. Unit cell determination and data reduction were carried out with the CrysAlisPro program (Rigaku). Empirical absorption correction was applied using spherical harmonics implemented in the SCALE3 ABSPACK scaling algorithm. This correction utilized symmetry-equivalent reflections combined with measurements at various azimuthal angles. Crystal structures were solved and refined against all F^2 values using the SHELXL and Olex2 software packages.[1,2] Anisotropic refinement was applied to the atomic displacement parameters of all non-hydrogen atoms, except for those within a disordered imidazolate ring in each structure, which were refined isotropically. Hydrogen atoms were placed in calculated positions, refined using a riding model with idealized geometries, and assigned fixed isotropic atomic displacement parameters. CCDC 2445903 contains the supplementary crystallographic data for this paper. These data can be obtained free of charge via www.ccdc.cam.ac.uk/conts/retrieving.html (or from the Cambridge Crystallographic Data Centre, 12 Union Road, Cambridge CB21EZ, UK; fax: (+44)1223-336-033; or deposit@ccdc.cam.ac.uk)

Powder X-ray Diffraction (PXRD). The samples were lightly ground in an agate mortar and pestle and used to fill 0.7 mm borosilicate capillaries that were mounted and aligned on an Brucker D8 Discover powder diffractometer, using Cu Kα radiation ($\lambda = 1.54056$ Å). The detector was an EIGER2 R 500K, multi-mode 2D. Pawley refinements were performed using TOPAS v6.0.[3]

Scanning Electron Microscopy (SEM): Scanning electron micrograph images were captured using the SCIOS 2 FIB-SEM. Samples were prepared by placing the powder on a carbon tape support and undergoing metallization before image collection. EDX analysis was conducted to examine the distribution of Mn^{2+} metal ion within the crystal structure.

Polarized Light Microscopy: Optical microscopy images of single grains of the different phases were acquired using a Nikon Eclipse LV-100 Optical microscope.

Thermogravimetric analysis (TGA): TGA measurements were conducted using a TGA 550 instrument (TA Instruments). All the samples were loaded in a platinum pan, under air or N_2 atmosphere. Initially, the sample was heated to 40 ºC and held isothermally for 15 minutes to stabilize. Subsequently, the sample was heated at a rate of 10 ºC min^{-1}.

Differential Scanning Calorimetry (DSC): DSC measurements were performed on a TRIOS DSC 250 instrument. Approximately 10-15 mg of the activated sample was loaded into a pierced-lid aluminum crucible (30 μL). An empty aluminum crucible served as the reference. Under a nitrogen atmosphere, the sample was heated to 40 °C and held isothermally for 15 minutes to ensure stabilization. Subsequently, the sample was heated to different final temperatures (300 °C for **MUV-44(dia-c)**, 400 °C for **MUV-44(zni)**, and 475 °C for **a_g-MUV-44**) at a heating rate of 10 °C min^{-1}. Upon reaching the target temperature, a 10-minute isotherm was performed to guarantee complete phase transition. Finally, the sample was cooled back to 25 °C at a rate of 10 °C min^{-1}.

X-ray Total Scattering: X-ray total scattering data were collected at room temperature using a PANalytical Empyrean laboratory diffractometer equipped with an Ag-K_α source and focusing mirrors. Samples were loaded into 1 mm diameter quartz glass capillaries and measured for over 24 hours each. Background scattering from an empty capillary and the diffractometer was also recorded. The resulting data were processed using the GudrunX[4] program to generate a normalized pair distribution function (PDF). The PDF was produced from the sine Fourier transform of $S(Q)$ using a Q-range of 0.6 to 18.5 Å^{-1} and was optimized such that the low-r region of the PDF function $G(r)$ oscillated around -1.

S2. Single crystal X-ray diffraction of MUV-44(mog)

Table S1 Crystallographic information of compound **MUV-44(mog)**.

Identification code	**MUV-44(mog)**
Empirical formula	$C_{24}H_{26}Mn_3N_{16}$
Formula weight	703.43
Temperature/K	120(2)
Crystal system	monoclinic
Space group	$P2_1/c$
a/Å	10.7686(5)
b/Å	12.9029(6)
c/Å	10.6640(4)
α/°	90
β/°	91.158(4)
γ/°	90
Volume/Å^3	1481.42(11)
Z	2
ρ_{calc}/g·cm^{-3}	1.577
μ/mm^{-1}	10.631
F(000)	714.0
Crystal size/mm^3	0.06 × 0.04 × 0.02
Radiation	Cu K_α (λ = 1.54184)
2Θ range for data collection/°	8.212 to 153.476
Index ranges	$-13 \leq h \leq 13$, $-15 \leq k \leq 6$, $-13 \leq l \leq 13$
Reflections collected	13940
Independent reflections	2999 [R_{int} = 0.0622, R_{sigma} = 0.0394]
Data/restraints/parameters	2999/0/196
Goodness-of-fit on F^2	1.024
Final R indexes [I>=2σ (I)]	R_1 = 0.0501 wR_2 = 0.1286
Final R indexes [all data]	R_1 = 0.0712 wR_2 = 0.1446
Largest diff. peak/hole / e Å^{-3}	0.70/–0.66

S3. Powder X-ray diffraction (PXRD)

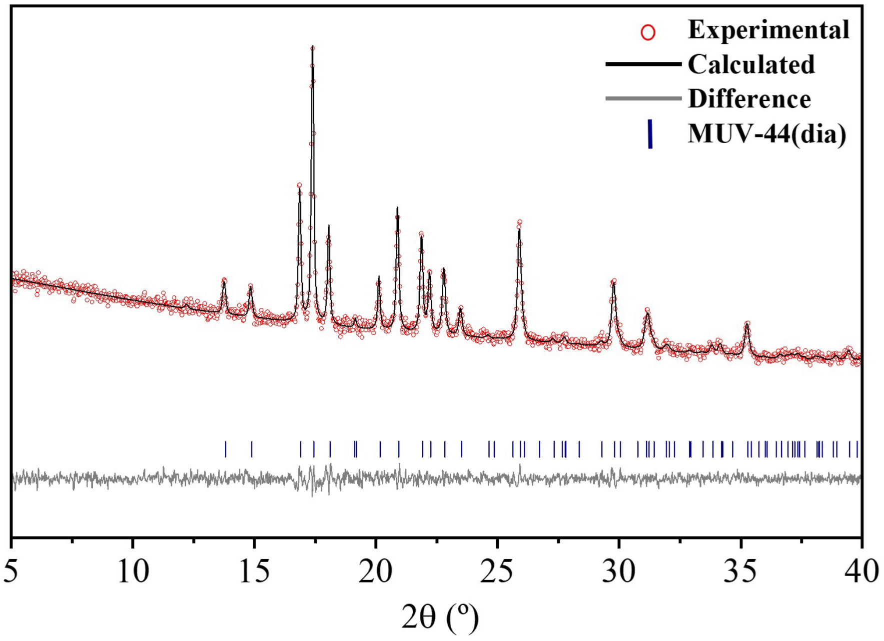

Figure S1. Pawley analysis of **MUV-44(dia-c)**. Experimental (red dots), calculated (black line), difference (grey line) and Bragg positions (ticks).

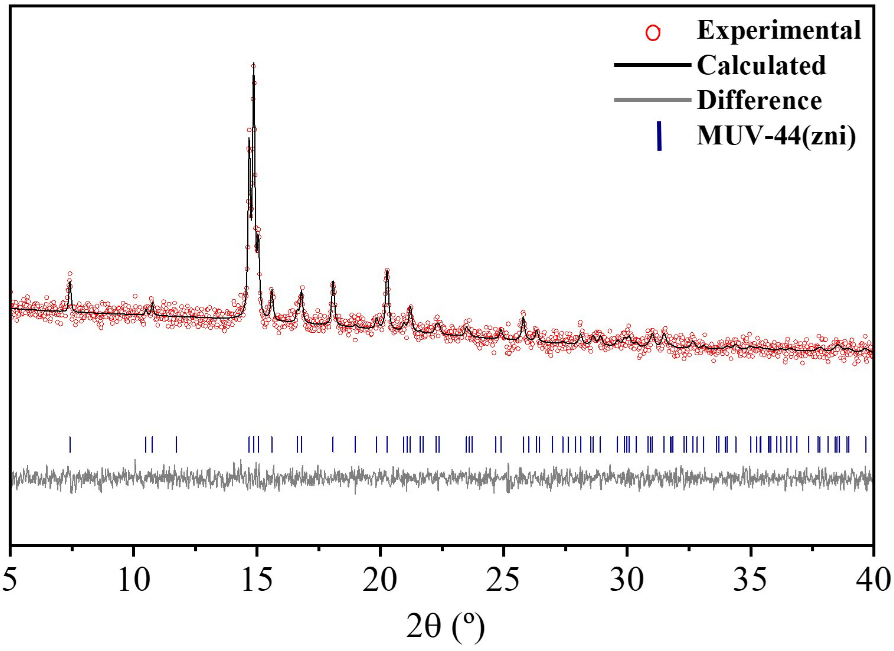

Figure S2. Pawley analysis of **MUV-44(zni)**. Experimental (red dots), calculated (black line), difference (grey line) and Bragg positions (ticks).

Table S2. Unit cell parameters of **MUV-44(dia-c)** and **MUV-44(zni)** extracted from Pawley refinements of the PXRD data compared with the values of the Zn analogues IMIDZB14 and XOMSIE extracted from the CCDC structures.

	a	***b***	***c***	***α***	***β***	***γ***	**Space group**
MUV-44(dia-c)	14.4286	10.4749	9.7888	90	90	90	*Pbca*
IMIDZB14	14.1163	10.5841	9.8646	90	90	90	*Pbca*
MUV-44(zni)	23.8157	23.8157	12.9104	90	90	90	$I4_1cd$
XOMSIE	23.4330	23.4330	12.4905	90	90	90	$I4_1cd$

S4. Stability test

Crystals of **MUV-44(mog)** were exposed to air under ambient conditions for variable durations. Subsequently, the materials underwent examination via X-ray powder diffraction. For **MUV-44(mog)** the diffraction peaks remained for two hours; after this period, a new phase began to emerge, and the material darkened.

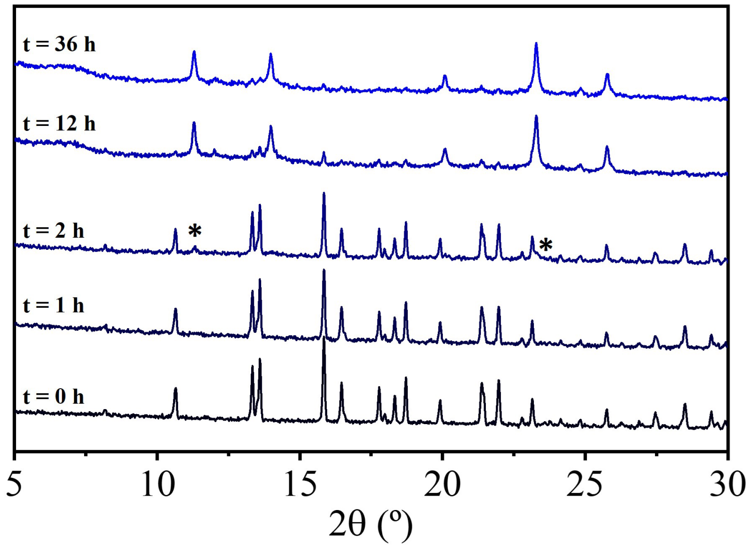

Figure S3. PXRD patterns of **MUV-44(mog)** at various air exposure times. The asterisk (*) indicates the appearance of the new phase, which is nearly fully formed after 12 hours.

S5. Differential scanning calorimetry (DSC)

DSC analyses show that successive upscans result in the formation of a vitreous phase, evidenced by the appearance of a glass transition at 176 °C. However, it is also observed that the material retains a melting transition, which diminishes with each subsequent cycle. We are confident that recrystallization does not occur, as no Bragg diffraction peaks are observed after the initial cycle. This suggests that the material may be transitioning into a vitreous phase as well as an amorphous state, and with each successive upscan, the glassy phase is becoming more purified.

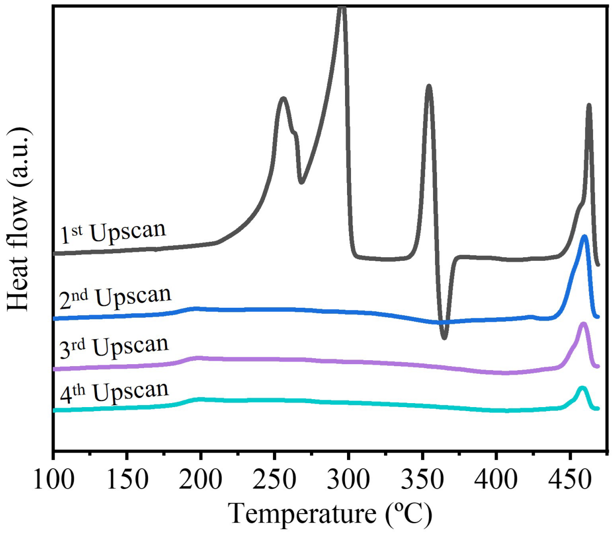

Figure S4. Successive DSC upscans of **MUV-44.**

S6. X-ray total scattering

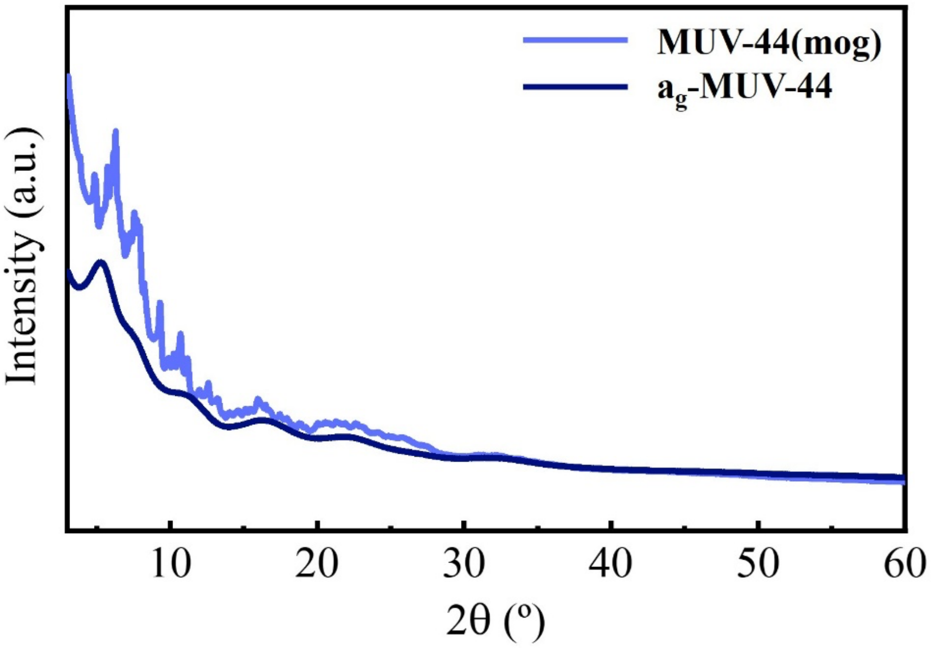

Figure S5. X-ray total scattering intensity data of **MUV-44(mog)** and **a$_g$-MUV-44**.

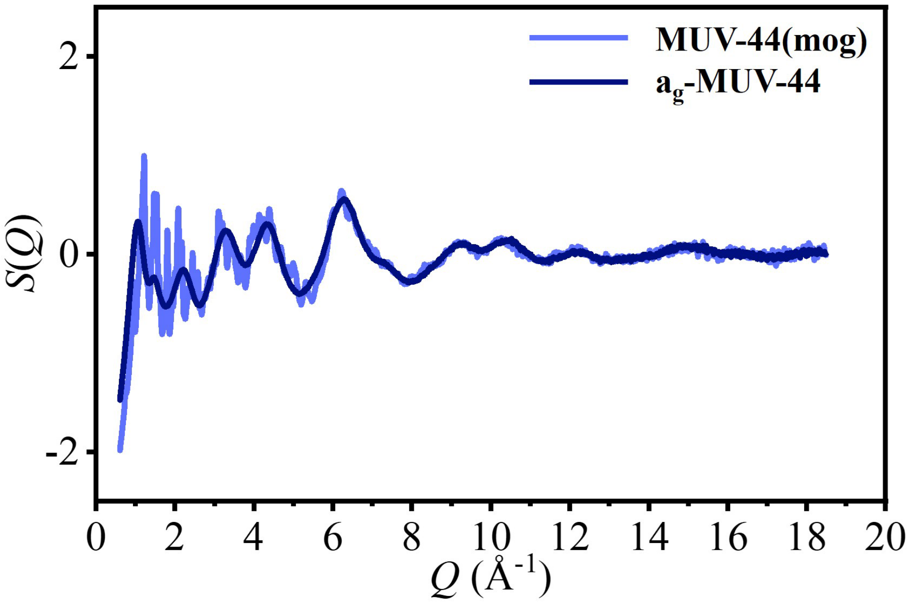

Figure S6. Total scattering structure factors, *S(Q)*, of **MUV-44(mog)** and **a$_g$-MUV-44**.

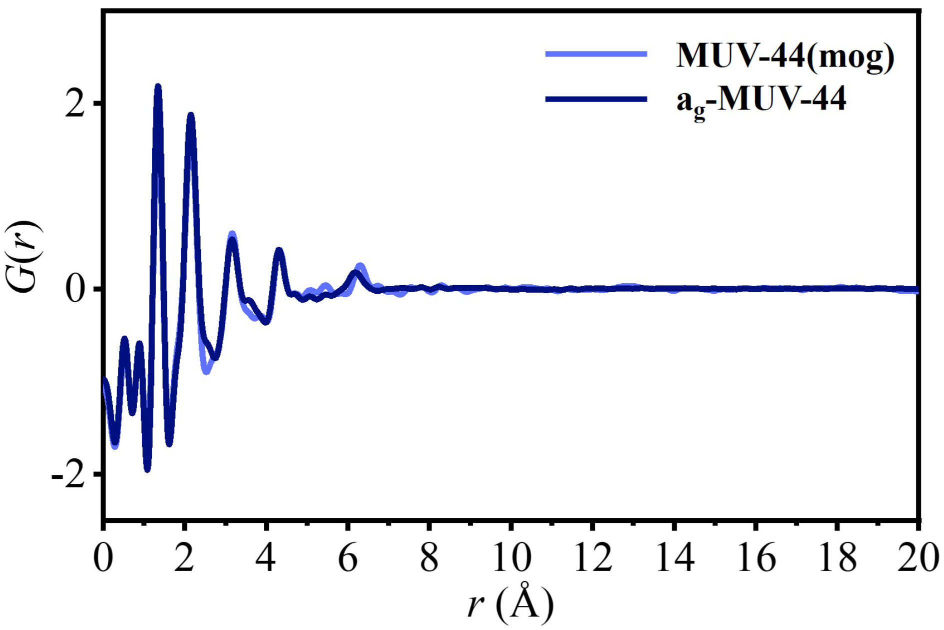

Figure S7. X-ray PDF in the form of $G(r)$ of **MUV-44(mog)** and **a_g-MUV-44**.

S7. Polarized light microscopy

Optical images were obtained with Nikin Eclipse LV-100 Optical microscope. Pictures of **MUV-44(mog)**, **MUV-44(dia-c)**, **MUV-44(zni)** and **a_g-MUV-44** are reported.

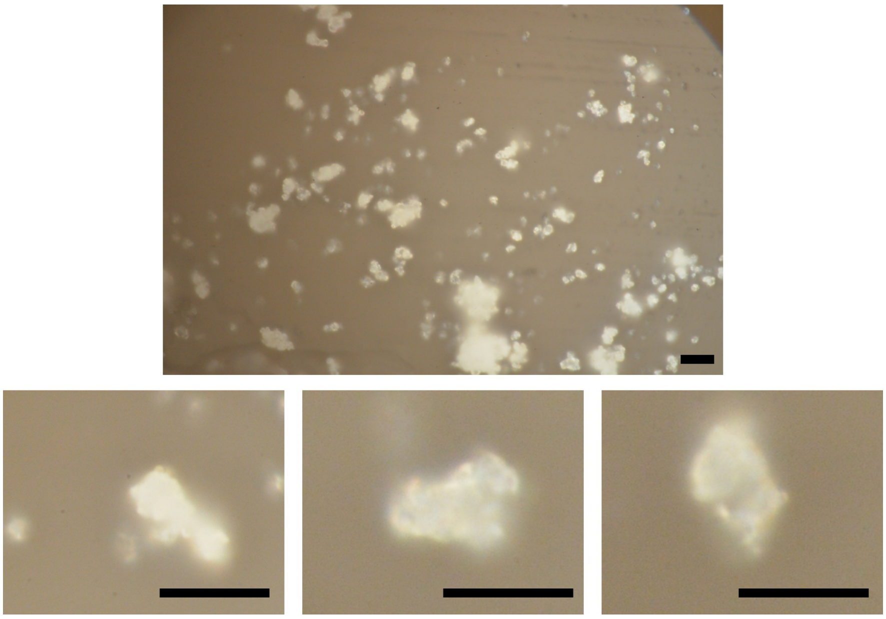

Figure S8. Optical images of different **MUV-44(mog)** crystals. Optical scale bars are 50 µm.

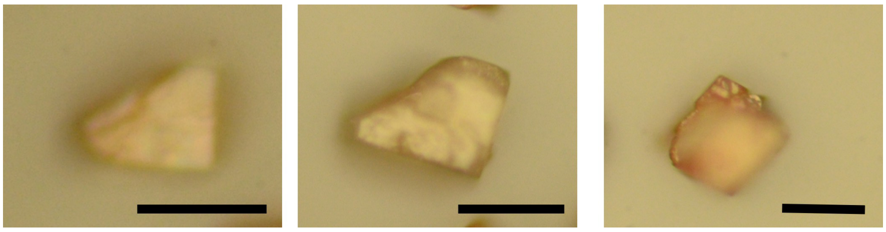

Figure S9. Optical images of different **MUV-44(dia-c)** samples. Optical scale bars are 50 µm.

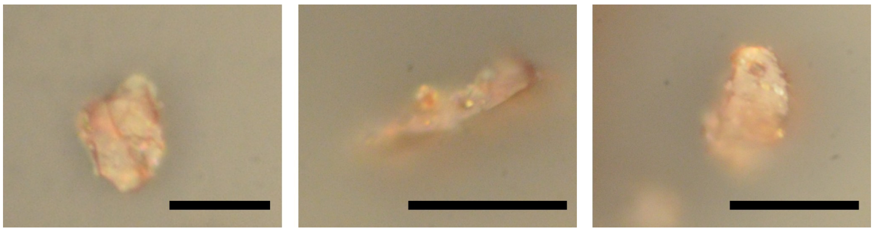

Figure S10. Optical images of different **MUV-44(zni)** samples. Optical scale bars are 50 μm.

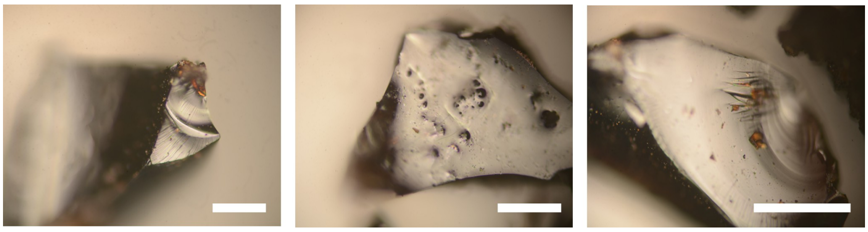

Figure S11. Optical images of different **a_g-MUV-44** samples. Optical scale bars are 50 μm.

S8. Scanning electron microscopy (SEM)

Scanning electron micrograph images were captured using the SCIOS 2 FIB-SEM. Samples were prepared by placing the powder on a carbon tape support and undergoing metallization before image collection. The synthesis conditions of the materials were established previously using DSC equipment.

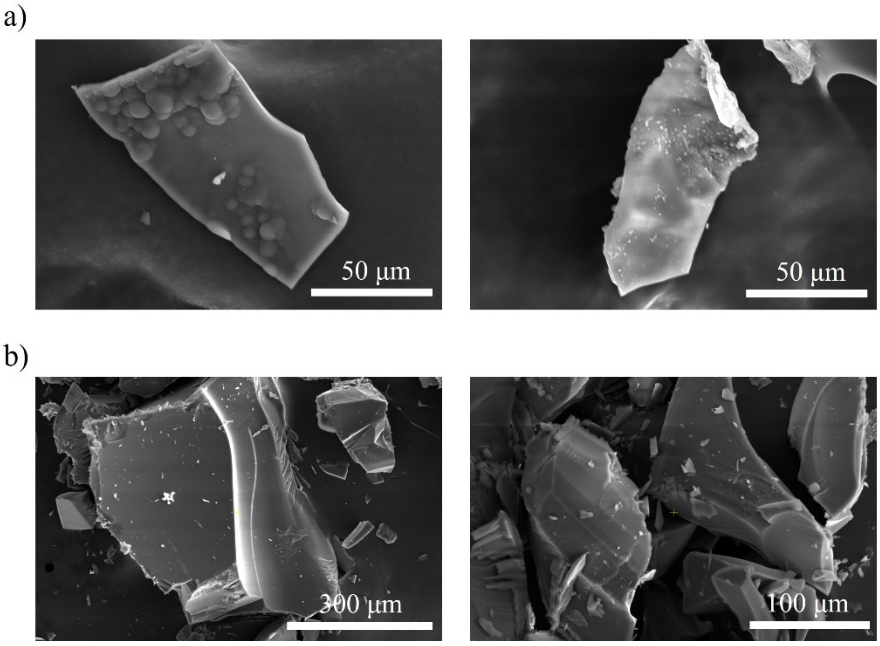

Figure S12. SEM images of a) **MUV-44(mog)** and b) **a_g-MUV-44**.

S9. Theoretical calculations

Crystal structure optimization of the **zni** topologies, including full relaxation of ionic positions and lattice parameters, were performed at DFT level in periodic boundary conditions, as implemented in the FHI-aims software.[5] The gradient-generalized approximation (GGA)-based PBEsol functional[6] and the tier-1 numeric atom-centered orbital (NAO) basis set with light settings, for all atoms, were used.

To perform molecular calculations, a neutral tetrahedron cluster was used: two deprotonated and two neutral imidazole ligands. The geometry was extracted from the optimized crystal structure for each system. [M(im)$_2$(Him)$_2$] (M = Zn, Fe, Mn; im = imidazolate; Him = imidazole). The Wiberg bond index (WBI) was calculated for all compounds. The WBI is a measure of the bond order calculated from the electron population overlap between two atoms.[7] Other bond order methodologies, like the Natural Atomic Orbital (NAO) index,[8] and the Intrinsic Bond Strength Index (IBSI),[9] were also calculated. In all bond strength indexes, a larger index value is related to a stronger bond, with reference values of 1, 2 and 3, for standard single, double and triple bond, respectively. As the nature of the chemical bond between the central metal and the neutral (Him) or charged (im$^-$) organic ligand is different, we calculated the indexes for both situations and report the average value for each index (see Table 1 in the main text). Finally, analysis of the coordination bond dissociation between the metal center and the nitrogen atom of a neutral imidazole molecule was carried out for each system by varying the M–N distance in a rigid scan. All the molecular calculations were performed at the hybrid-DFT HSE06/def2-SVPP[10] level of theory using the Gaussian-16.A03 program suite.[11]

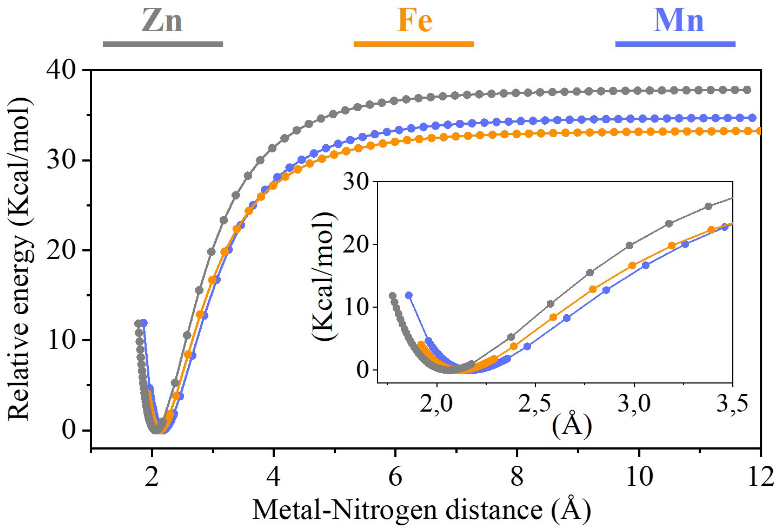

Figure S13. Metal–N bond dissociation energy profile calculated for the secondary building unit cluster of Zn^{2+}, Fe^{2+} and Mn^{2+} ZIFs (**zni** topology) using the HSE06/def2-SVPP level of theory.

S10. References

(1) G. M. Sheldrick, SHELXT − Integrated space-group and crystal-structure determination. *Acta Cryst.* **2015**, *71*, 3−8.

(2) O. V. Dolomanov, L. J. Bourhis, R. J. Gildea, J. A. K. Howard, H. Puschmann, OLEX2: a complete structure solution, refinement and analysis program. *J. Appl. Cryst*. **2009**, *42*, 339−341.

(3) Coelho, A. A. TOPAS and TOPAS-Academic: an optimization program integrating computer algebra and crystallographic objects written in C^{++}. *J. Appl. Cryst.* **2018**, *51*, 210–218.

(4) A. K. Soper, GudrunN and GudrunX: programs for correcting raw neutron and X-ray diffraction data to differential scattering cross section, science & technology facilities council, **2011**.

(5) V. Blum, R. Gehrke, F. Hanke, P. Havu, V. Havu, X. Ren, K. Reuter, M. Scheffler, Ab initio molecular simulations with numeric atom-centered orbitals, *Comput. Phys. Commun.*, **2009**, 180, 2175-2196,

(6) J. P. Perdew, A. Ruzsinszky, G. I. Csonka, O. A. Vydrov, G. E. Scuseria, L. A. Constantin, X. Zhou, K. Burke. Restoring the Density-Gradient Expansion for Exchange in Solids and Surfaces. *Phys. Rev. Lett.*, **2008**, *100*, 136406.

(7) Y. Ge, A. Le, G. J. Marquino, P. Q. Nguyen, K. Trujillo, M. Schimelfenig, A. Noble. Tools for Prescreening the Most Active Sites on Ir and Rh Clusters toward C–H Bond Cleavage of Ethane: NBO Charges and Wiberg Bond Indexes. *ACS Omega* **2019**, *4*, 18809-18819.

(8) A. E. Reed, F. Weinhold. Natural bond orbital analysis of near-Hartree–Fock water dimer. *J. Chem. Phys*., **1983**, *78*, 4066–4073.

(9) J. Klein, H. Khartabil, J.C. Boisson, J. Contreras-García, J. P. Piquemal, E. Hénon. New Way for Probing Bond Strength. *J. Phys. Chem. A*, **2020,** *124*, 1850-1860.

(10) A. V. Krukau, O. A. Vydrov, A. F. Izmaylov, G. E. Scuseria. Influence of the exchange screening parameter on the performance of screened hybrid functionals. *J. Chem. Phys.*, **2006**, *125*, 224106.

(11) Gaussian 16, Revision C.01, Frisch, M. J.; Trucks, G. W.; Schlegel, H. B.; Scuseria, G. E.; Robb, M. A.; Cheeseman, J. R.; Scalmani, G.; Barone, V.; Petersson, G. A.; Nakatsuji, H.; Li, X.; Caricato, M.; Marenich, A. V.; Bloino, J.; Janesko, B. G.; Gomperts, R.; Mennucci, B.; Hratchian, H. P.; Ortiz, J. V.; Izmaylov, A. F.; Sonnenberg, J. L.; Williams-Young, D.; Ding, F.; Lipparini, F.; Egidi, F.; Goings, J.; Peng, B.; Petrone, A.; Henderson, T.; Ranasinghe, D.; Zakrzewski, V. G.; Gao, J.; Rega, N.; Zheng, G.; Liang, W.; Hada, M.; Ehara, M.; Toyota, K.; Fukuda, R.; Hasegawa, J.; Ishida, M.; Nakajima, T.; Honda, Y.; Kitao, O.; Nakai, H.; Vreven, T.; Throssell, K.; Montgomery, J. A., Jr.; Peralta, J. E.; Ogliaro, F.; Bearpark, M. J.; Heyd, J. J.; Brothers, E. N.; Kudin, K. N.; Staroverov, V. N.; Keith, T. A.; Kobayashi, R.; Normand, J.; Raghavachari, K.; Rendell, A. P.; Burant, J. C.; Iyengar, S. S.; Tomasi, J.; Cossi, M.; Millam, J. M.; Klene, M.; Adamo, C.; Cammi, R.;

Ochterski, J. W.; Martin, R. L.; Morokuma, K.; Farkas, O.; Foresman, J. B.; Fox, D. J. Gaussian, Inc., Wallingford CT, 2016.